Solid lithium electrolyte-Li$_4$Ti$_5$O$_{12}$ composites as anodes of lithium-ion batteries showing high-rate performance

Yujing Sha [a], Tao Yuan [a], Bote Zhao [a], Rui Cai [a], Huanting Wang [b], Zongping Shao [a,b,∗]

[a] State Key Laboratory of Materials-Oriented Chemical Engineering, College of Chemistry & Chemical Engineering, Nanjing University of Technology, Nanjing 210009, China
[b] Department of Chemical Engineering, Monash University, Australia

HIGHLIGHTS

► Solid lithium electrolyte–Li$_4$Ti$_5$O$_{12}$ composite anode was prepared facilely.
► La-incorporated Li$_4$Ti$_5$O$_{12}$ is dense but with high lithium electroactivity.
► Rich dual phase boundaries induce pseudocapacitive effect.
► La-incorporated Li$_4$Ti$_5$O$_{12}$ anode showed a high capacity of 113.5 mA h g^{-1} at 40 C.

ARTICLE INFO

ABSTRACT

A new concept lithium-ion conducting lithium lanthanum titanate solid electrolyte and Li$_4$Ti$_5$O$_{12}$ composite is proposed as efficient anode of lithium-ion batteries with outstanding rate performance, which can be facilely prepared by one-pot combustion technique. The as-synthesized composites are in micrometer size with dense nature which effectively reduces the electrode-liquid electrolyte interface area, thus decreasing irreversible capacity during the first charge–discharge cycle and prolonging cycling stability. However, the composites are rich in lithium lanthanum titanate and Li$_4$Ti$_5$O$_{12}$ dual phase boundaries due to intimate nanoscale mixing of the two phases. The apparent lithium-ion conductivity of the composite electrode gets significantly improved as compared to pristine Li$_4$Ti$_5$O$_{12}$ due to the incorporation of lithium lanthanum titanate phase, a high lithium ionic conductor. As a result, the as-synthesized composites show a high capacity of 113.5 mA h g^{-1} even at a discharge rate of 40 C, more than 200% that of a pristine Li$_4$Ti$_5$O$_{12}$. The concept is general, which may also be applicable to other electrode materials, and it thus introduces a new way for the development of high rate-performance electrodes for lithium-ion batteries.

1. Introduction

The air pollution and greenhouse effect due to the emissions from vehicles with internal combustion engines have become serious problems of our modern society, especially in urban areas. For a more sustainable future, electric vehicles (EVs) and hybrid electric vehicles (HEVs), which produce less or even zero pollutant and CO$_2$, have received tremendous yet increasing attention from both the public and governments all over the world [1–6]. The success in such green vehicles, however, relies strongly on the development of storage batteries system. To this end, lithium-ion batteries are believed the most promising candidate due to their high energy density, no memory effect, light weight, environmental benignity, and high voltage [7–11].

Spinel-type Li$_4$Ti$_5$O$_{12}$ oxide is a potential anode material for such lithium-ion batteries, which shows several outstanding character-istics, such as near zero volumetric change during the lithium electrochemical insertion and extraction processes ensuring a long cycling lifetime, a very flat voltage platform at around 1.55 V vs Li$^+$/Li well above the potential for metallic lithium formation ensuring good operational safety, and a high thermal stability [10,12,13]. Although it has an affordable theoretical discharge capacity of ∼175 mA h g^{-1}, the actual capacity at high discharge rate for electrode made from coarse Li$_4$Ti$_5$O$_{12}$ powder is often much lower because of large polarization resistance originated from the poor bulk diffusion properties [14]. Improving the rate performance of

$Li_4Ti_5O_{12}$ is thus of critical importance to realize its successful application in EVs and HEVs.

Reducing the particle size will effectively shorten the diffusion distance for both lithium ion and electron as well as increase the surface area for interfacial reaction; consequently, the polarization resistances associated with both the surface reaction and bulk diffusion may be effectively reduced [15–19]. Many reports have shown excellent rate performance of $Li_4Ti_5O_{12}$ nano powder [20–24]. However, the current collection of nano electrode was turned out to be fairly difficult. In addition, the high surface area of nanometer-sized electrode materials may also increase the reaction rate with liquid electrolyte and additives because of large liquid electrolyte/electrode interface, thus reducing the cell lifetime and increasing the irreversible capacity in the first discharge–charge cycle. To improve the current collection, several researchers have tried to prepare hierarchical nano-porous $Li_4Ti_5O_{12}$ microspheres through advanced synthetic techniques [25,26]. However, the drawbacks associated with the high surface area are still not solved. In addition, the high porosity may also introduce low tap density. For example, Shen et al. prepared porous $Li_4Ti_5O_{12}$ microspheres as anode of lithium-ion batteries by a hydrothermal method. Although outstanding rate performance was reported, the large pore volume of 0.871 cm^3 g^{-1} resulted in relative density of the spheres of only 25.8%, even assuming cubic close packing of those spheres the tap density is still only 0.863 g cm^{-3}, which is too low to have practical importance [25]. On the other hand, the synthetic process is typically composed of multisteps in order to obtain such complex morphology, which increases the fabrication cost, making it economically less attractive.

Herein, we report outstanding rate performance can also be reached for pore-free micrometer-sized La-incorporated $Li_4Ti_5O_{12}$ with low specific surface area. In particular, we propose a new concept of solid lithium-conducting electrolyte-$Li_4Ti_5O_{12}$ composites as electrodes of lithium-ion batteries, which can be prepared by a facile technique based on one-pot combustion synthesis. A capacity of 113.5 mA h g^{-1} was successfully obtained even at a high discharge rate of 40 C for a coarse pore-free electrode with a specific surface area of only 5.9 m^2 g^{-1}. Furthermore, the electrode shows fairly stable cycling stability. The concept is general, which may also be applicable to other electrode materials such as $LiFePO_4$ to overcome their drawbacks of poor surface kinetics and poor lithium bulk diffusion. It thus introduces a new way for the development of high rate-performance electrodes for lithium-ion batteries.

2. Experimental

2.1. Material preparation

The La-incorporated $Li_4Ti_5O_{12}$ with different La to Ti molar ratios was synthesized by a one-pot cellulose-assisted combustion method [27]. During the synthesis, analytical reagents of lithium nitrate ($LiNO_3$) (AR), lanthanum nitrate ($La(NO_3)_3 \cdot 6H_2O$) (AR) and tetrabutyl titanate ($Ti(C_4H_9O)_4$) (CP) were used as the cation sources, all of which were used as received without further purification or treatment. De-seeded natural cotton fiber was applied as the cellulose source which was activated with HNO_3 before use. The typical procedure for the combustion synthesis was shown schematically in Fig. 1. De-ionized water was slowly dropped into $Ti(C_4H_9O)_4$ under vigorously stirring, leading to the formation of white precipitate of $TiO(OH)_2$. Nitric acid was then introduced under stirring with ice-water bathing to result in a transparent bright yellow titanyl nitrate solution. Proper amounts of $LiNO_3$, $La(NO_3)_3 \cdot 6H_2O$ and glycine were added slowly into the solution in sequence. The mixed solution was then absorbed into dried

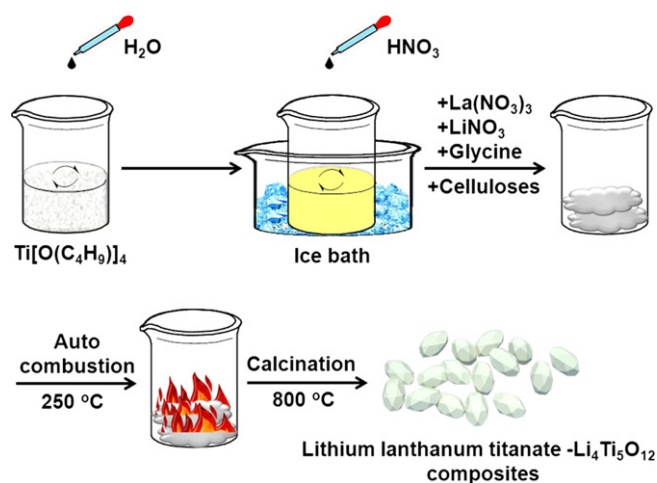**Fig. 1.** Schematic illustration for the synthesis of lithium lanthanum titanate–$Li_4Ti_5O_{12}$ composite.

activated cotton fibers. After drying at around 80 °C, the solid precursor was further heated at 250 °C in an electric oven, a high temperature self-combustion with the appearance of strong flame was triggered which lasted for 10–15 s and a gentle combustion was followed which lasted for several minutes. More specifically, for one single combustion synthesis, we took 0.050 mol $Ti(C_4H_9O)_4$, 0.043 mol $LiNO_3$ (excessive 8% mole ratio allowing for the lithium volatilization at 800 °C), 0.15 mol glycine and specific mole of $La(NO_3)_3 \cdot 6H_2O$ according to different La to Ti mole ratios (1:500, 1:250, 1:150, 1:100, 1:50) as raw materials. We also prepared pristine $Li_4Ti_5O_{12}$ sample by the same combustion synthesis technique. The as-obtained primary products were in gray color and took the original cotton fiber morphologies, which were grinded and subjected for further calcinations at 800 °C for 5 h to result in the final products.

2.2. Material characterization

The phase structure of as-prepared La-incorporated $Li_4Ti_5O_{12}$ with different La to Ti molar ratios was characterized by X-ray diffraction (XRD, Bruker D8 advance diffractometer with filtered Cu Kα radiation, λ = 0.15406 nm). The particle size and particulate morphology of the products were characterized by Environmental Scanning Electron Microscopy (ESEM, HITACHI S-4800) and Transmission Electronic Microscopy (TEM, JEOL JEM-2100). The specific surface area of the samples was obtained by N_2 adsorption at the temperature of liquid nitrogen by the BELSORP II instrument after being pretreated at 250 °C. Moreover, to obtain the chemical information of oxide surface, angle resolved X-ray photoelectron spectroscopy (XPS) analysis was carried out. The XPS was obtained using a PHI spectrometer (model 550) equipped with an Al mode source.

2.3. Electrochemical test

The working electrodes were composed of active material, conductive Super P (NCM HERSBIT Chemical Co., LTD., China), PVDF (polyvinylidene fluoride, Aldrich) (85:8:7 in weight) in NMP (N-methyl-2-pyrrolidone). Electrode slurry was first prepared, which was then deposited on current collectors of copper foil by blading. Disk-shape pieces of slurry-covered Cu foil were dried in a vacuum at 100 °C for 12 h. Then the half cells were assembled with the disk-shape electrode as the working electrode, metallic

lithium film as the reference electrode and also the counter electrode, and a mixture solution composed of 1 mol L^{-1} LiPF$_6$ and ethylene carbonate (EC)/diethyl carbonate (DMC) (1:1 by volume) as the electrolyte. A microporous polypropylene film (Celgard 2400) was used as the separator. The assembly process was conducted in a glove box filled with pure argon atmosphere.

The charge–discharge characteristics of the cells were recorded over the potential range between 1.0 and 3.0 V using a NEWARE BTS-5 V 50 mA computer-controlled battery test station. Cyclic voltammetry tests were performed over the potential range of 1.0–3.0 V using a Princeton Applied Research PARSTAT 2273 advanced electrochemical system at the scanning rate of 0.1, 0.2, 0.5, 1.0, 2.0 mV s^{-1}, respectively. Complex impedance measurements were also carried out with Princeton 2273 electrochemical system over the single cell at the state of discharging (1.6 V). A perturbation of 10 mV was applied and we collected data under PC control at the frequency range of 1 MHz–100 mHz. To test the electronic conductivity of the as-prepared samples, the powder was pressed into bars by a stainless steel mold under a hydraulic pressure of approximately 1.5×10^8 Pa and further sintered at 800 °C at a heating rate of 5 °C min^{-1}. Four-probe direct current (DC) conductivity measurement was conducted at room temperature using a Keithley

2420 digital source meter on bar-shape pellets applying silver paste as the electrodes.

3. Results and discussion

3.1. Particulate morphology

Fig. 2 shows the typical SEM images of activated cellulose fibers, cellulose fibers after the impregnation with metal nitrates and glycine fuel, a typical primary product from the auto combustion, and a final product with different La to Ti molar ratios after the further calcination at 800 °C in air. The activated cotton fibers are in flat tube shape; after the impregnation with metal nitrates and glycine fuels, the fibers became robust, suggesting the successful absorption of the nitrates and glycine into the lumens and pores of the cotton fibers. The primary product from the auto combustion still took the morphology of activated cotton fiber. However, after grinding and further calcinations at 800 °C the products were seriously sintered, which are composed of irregular shape grains with the size mainly in the range of 0.20–1.00 μm. The increase of La content did not have obvious effect on the particle size and the degree of particles aggregation.
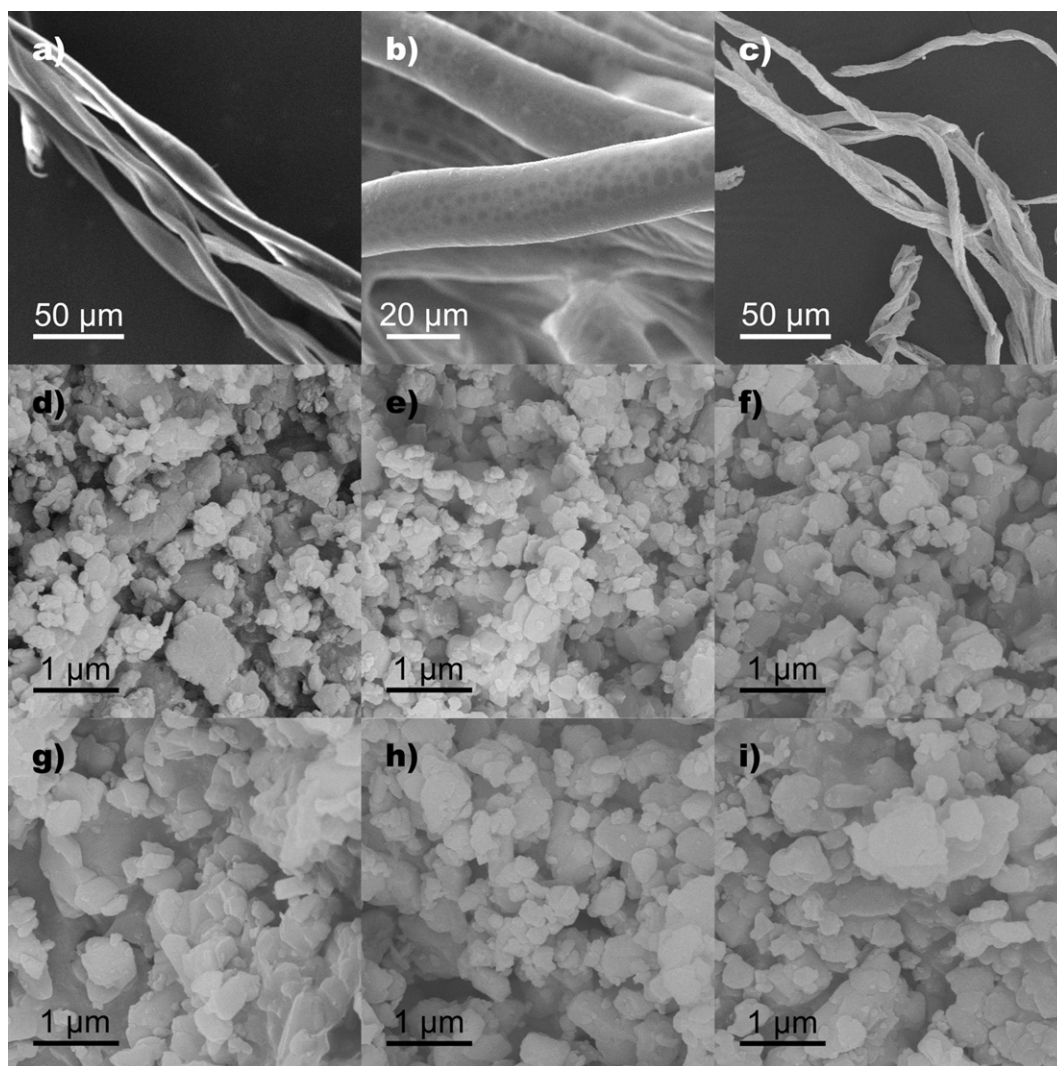
Fig. 2. The SEM images of (a) activated cellulose; (b) cellulose-GN precursor; (c) cellulose after 250 °C self-combustion and the final products with different La to Ti ratios: (d) pure Li$_4$Ti$_5$O$_{12}$; (e) La:Ti = 1:500; (f) La:Ti = 1:250; (g) La:Ti = 1:150; (h) La:Ti = 1:100; (i) La:Ti = 1:50.

To get more details about the particulate morphologies, the samples were further examined by TEM. As shown in Fig. 3, the primary particles of the pristine $Li_4Ti_5O_{12}$ and La-incorporated $Li_4Ti_5O_{12}$ (La:Ti = 1:50) have the size mainly in the range of 0.05–0.35 μm. However, those primary particles showed obvious fusion to form large aggregates with the size in the micrometer level, in well agreement with the observation of large secondary grains in the range of 0.2–1.0 μm by SEM (Fig. 2).

The specific surface areas, pore size and distribution of the prepared materials were determined by nitrogen isothermal adsorption–desorption measurements using the Brunauer–Emmett–Teller (BET) method. The specific surface areas were found to be only 1.4, 3.7, 4.0, 4.8, 5.3 and 5.9 m^2 g^{-1} for pristine $Li_4Ti_5O_{12}$, and La-incorporated $Li_4Ti_5O_{12}$ with La to Ti molar ratios of 1:500, 1:250, 1:150, 1:100 and 1:50, respectively. It further demonstrated that the as-prepared samples were in coarse type. Fig. 4a shows the typical nitrogen adsorption–desorption curve of a La-incorporated $Li_4Ti_5O_{12}$ (La:Ti = 1:50), and Fig. 4b exhibits the pore size distribution curve of the above-mentioned sample. There existed almost neither any micropores nor nanopores in the sample with the pore volume of only 0.023 cm^3 g^{-1}, in well accordance with the TEM observation. Similar negligible pore volumes were observed for the other samples. It further demonstrated that the micrometer-sized particles were well densified, which is beneficial to achieve high packing density of the electrode, thus ensuring high volumetric energy density of the corresponding batteries. Assuming the spheric shape of the particles and total contribution of the surface area from outer surface of the particles, the estimated diameter of the spheres for the samples with the La to Li ratios of 0:500, 1:500, 1:250, 1:150, 1:100 and 1:50 was found to be 1.253, 0.474, 0.438, 0.365, and 0.297 μm, respectively, which matched properly with the SEM observation while they were larger than the sizes of primary particles, it further supports the dense nature of the secondary particles prepared from the combustion synthesis.

3.2. Phase composition

To detect phase composition, the various La-incorporated $Li_4Ti_5O_{12}$ samples prepared from the combustion synthesis were first examined by room-temperature XRD patterns with the results shown in Fig. 5. At relatively low La to Ti molar ratios, i.e., 1:500, 1:250 and 1:150, seven diffraction peaks successively appeared at the 2θ of 18.4, 35.6, 43.3, 47.4, 57.2, 62.8 and 66.1°, which can be well assigned to the characteristic diffraction peaks of the face-centered cubic $Li_4Ti_5O_{12}$-related spinel phase with the $Fd\bar{3}m$

space group at the planes of (111), (311), (400), (331), (333), (440) and (531), respectively (JCPDS Card No. 49-0207). No any impurity phase was observed within the detection limit of XRD. However, with the further increase of La to Ti molar ratio to 1:100, in addition to those peaks for the spinel phase an additional diffraction peak at around $2\theta = 33°$ appeared and a second additional peak at 2θ around 58° also appeared at La to Ti molar ratio of 1:50, which can be assigned to the formation of perovskite type lithium lanthanum titanate phase, a promising solid lithium-ion conducting electrolyte with high conductivity [28,29]. It further supports that the La-incorporated $Li_4Ti_5O_{12}$ samples prepared from the combustion synthesis are actually composed of a mixture of lithium lanthanum titanate perovskite and $Li_4Ti_5O_{12}$ spinel phase, at least for the samples with high La to Ti molar ratios.

To get further structural information about the as-synthesized La-incorporated $Li_4Ti_5O_{12}$ samples, they were also examined by HR-TEM. Fig. 6 shows the typical HR-TEM image and SAED figure of a primary particle of La-incorporated $Li_4Ti_5O_{12}$ with a La to Ti molar ratio of 1:50. The individual primary particle showed two types of diffraction fringes with the fringe spaces of 0.483 (mark A) and 0.272 nm (mark B), which can be assigned to the (111) diffraction plane of $Li_4Ti_5O_{12}$ spinel phase and a typical diffraction plane of lithium lanthanum titanate perovskite phase (diffraction plane of (110) or (102)), respectively. The corresponding SAED as shown in Fig. 6b also indicated two types of rings, assignable to $Li_4Ti_5O_{12}$ spinel and lithium lanthanum titanate perovskite phases respectively; it further supports that the as-obtained samples from the combustion synthesis are composed of $Li_4Ti_5O_{12}$ and lithium lanthanum titanate dual phases. Thus, the submicrometer-sized primary particles are actually composed of $Li_4Ti_5O_{12}$ and lithium lanthanum titanate dual phases in nanoscale with rich two-phase boundaries.

It is well known that many elements can be doped into the 8a Li^+ tetrahedral sites or 16d octahedral sites of $Li_4Ti_5O_{12}$ [30–35]. Thus, in addition to the formation of new lithium lanthanum titanate phase, La may also be doped into the lattice structure of $Li_4Ti_5O_{12}$. The lattice parameters of the spinel phase in the composites were then determined using the Bragg Formula by fitting the diffraction peaks at (111) index plane. Values of 8.321(3), 8.318(2), 8.317(3), 8.316(1), 8.315(3) and 8.314(2) Å were obtained for pristine $Li_4Ti_5O_{12}$ and La-incorporated $Li_4Ti_5O_{12}$ with La to Ti molar ratios of 1:500, 1:250, 1:150, 1:100 and 1:50, respectively. It is very interesting that the lattice was shrunk with increasing La^{3+} content. Li^+ and Ti^{4+} have an ionic radius of 0.59/0.76 Å and 0.42/0.605 Å at the 8a tetrahedral site/16d octahedral site, respectively [36], while La^{3+} typically has larger

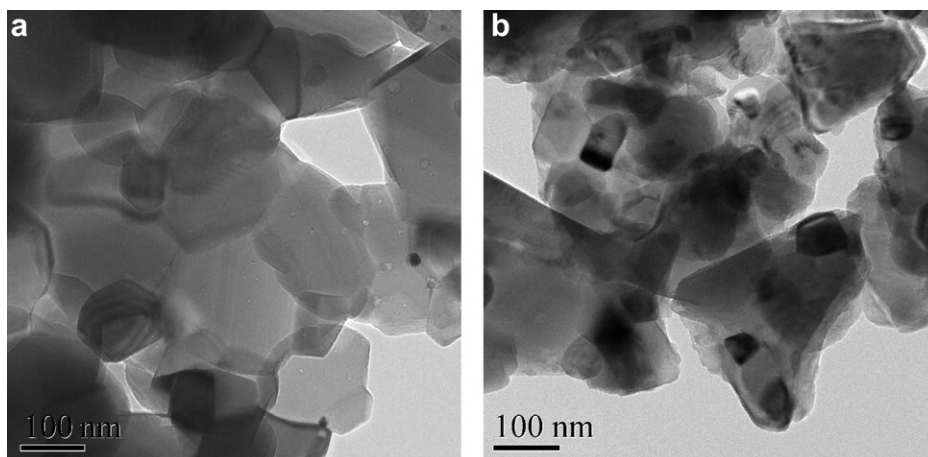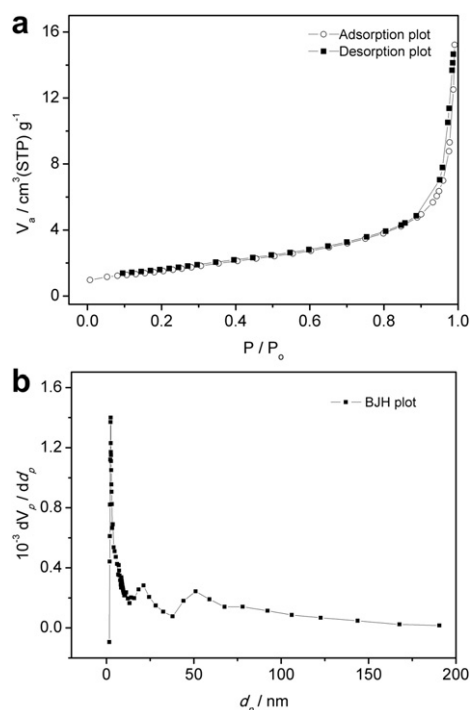**Fig. 3.** TEM images of as-prepared (a) pure $Li_4Ti_5O_{12}$; (b) La-incorporated $Li_4Ti_5O_{12}$ (La:Ti = 1:50).

Fig. 4. (a) The typical nitrogen adsorption–desorption curve of a La-incorporated $Li_4Ti_5O_{12}$ (La:Ti = 1:50), and (b) the pore size distribution curve of the sample.

cation size than both Li^+ and Ti^{4+}. A lattice expansion should be expected with the doping of La^{3+} into either the 8a tetrahedral or 16d octahedral site of the $Li_4Ti_5O_{12}$ lattice. We thus assume that the doping of La^{3+} into $Li_4Ti_5O_{12}$ lattice likely induced the displacement of partial Ti^{4+} from the 16d octahedral site to the 8a tetrahedral site.

It is well known that the doping of cations with high oxidation state into the 8a Li^+ tetrahedral sites would result in an increase in the electronic conductivity due to the increase of electron hole concentration [37], while the presence of lithium lanthanum titanate would reduce the electronic conductivity since it is a pure lithium-ion conductor. The electronic conductivity of the various La-incorporated $Li_4Ti_5O_{12}$ samples was measured by four-probe DC method using lithium-ion blocking silver electrodes. The values of 1.12×10^{-8}, 2.46×10^{-8}, 2.2×10^{-8}, 1.93×10^{-8}, 2.64×10^{-8} and 2.48×10^{-8} S cm^{-1} were found for pristine $Li_4Ti_5O_{12}$ and La-incorporated $Li_4Ti_5O_{12}$ composites with La to Ti molar ratios of 1:500, 1:250, 1:150, 1:100 and 1:50, respectively. The slightly higher electronic conductivity for the La-incorporated $Li_4Ti_5O_{12}$
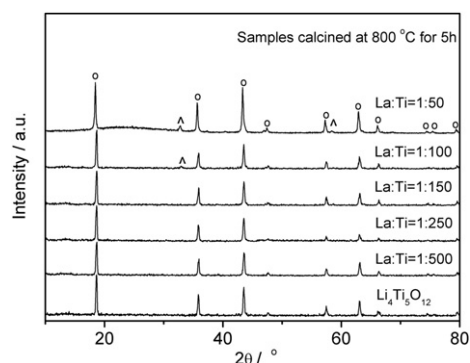

Fig. 5. XRD patterns of as prepared pure $Li_4Ti_5O_{12}$ and La-incorporated with different La to Ti ratios of 1:500, 1:250, 1:150, 1:100 and 1:50 respectively; "o" spinel $Li_4Ti_5O_{12}$, "∧" perovskite lithium lanthanum titanate phase.

than pristine $Li_4Ti_5O_{12}$ suggests the partial displacement of Ti^{4+} into the 8a site indeed happened in La-incorporated $Li_4Ti_5O_{12}$. We further analyzed the oxidation states of titanium in the pristine $Li_4Ti_5O_{12}$ and La-$Li_4Ti_5O_{12}$ (La:Li = 1:50) by XPS with the results shown in Fig. 7. The binding energies in the XPS analysis were corrected for specimen charging by referencing the C 1s line to 284.5 eV. For both the pristine $Li_4Ti_5O_{12}$ and La-$Li_4Ti_5O_{12}$ (La:Ti = 1:50), the XPS of Ti^{4+} 2p matched pretty well with the commercial TiO_2. It means the Ti in both samples took Ti^{4+} oxidation state. Thus the Ti^{4+} valence state change due to the La doping into $Li_4Ti_5O_{12}$ lattice is actually weak, agreeing well with the only slightly improved electronic conductivity by La incorporation.

3.3. Electrode performance

The performance of as-synthesized coarse La-incorporated $Li_4Ti_5O_{12}$ samples was first characterized by constant current charge–discharge tests at 1 C rate between 1.0 and 3.0 V using the composites as working electrode and metallic lithium as the counter as well as the reference electrode. As illustrated in Fig. 8, the first discharge capacity reached 167.0, 168.0, 177.5, 177.2, 170.3 and 168.7 mA h g^{-1} for pristine $Li_4Ti_5O_{12}$ and La-incorporated $Li_4Ti_5O_{12}$ with La to Ti molar ratios of 1:500, 1:250, 1:150, 1:100 and 1:50, respectively, which are all nearly the theoretical capacity of bulk $Li_4Ti_5O_{12}$ (175 mA h g^{-1}). A slight increase in discharge capacity with the increase of La to Ti molar ratio was observed for the electrodes when it was less than 1:150, likely due to the increased surface area and electronic conductivity of the electrode material. However, with the further increase of La to Ti ratio, a gradual decrease in discharge capacity was observed, it can be explained by the reduced amount of spinel phase in the composite, which performed as the active material for lithium storage. For all electrodes, high coulombic efficiency of larger than 95% was reached in the first discharge–charge cycle, and the coulombic efficiency started to reach almost 100% from the second cycle on. The irreversible capacity for the first charge–discharge process may be resulted from the dissolution of impurity phase from the electrodes surface [38]. In addition, as
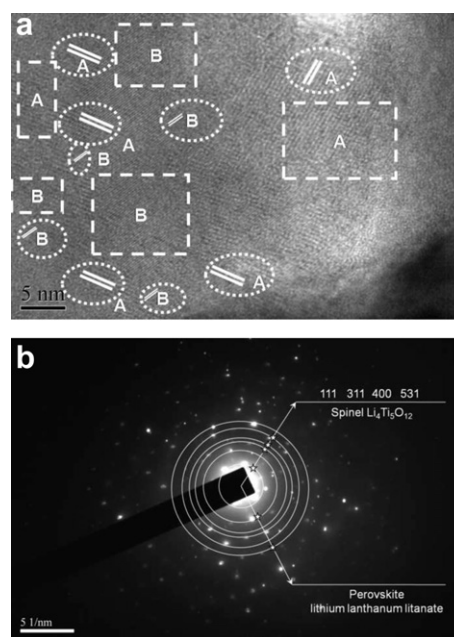
Fig. 6. (a) Typical HR-TEM images (mark A and B present $Li_4Ti_5O_{12}$ spinel phase and lithium lanthanum titanate perovskite phase respectively) and (b) SAED of La-incorporated $Li_4Ti_5O_{12}$ with La-to-Li molar ratio of 1:50.

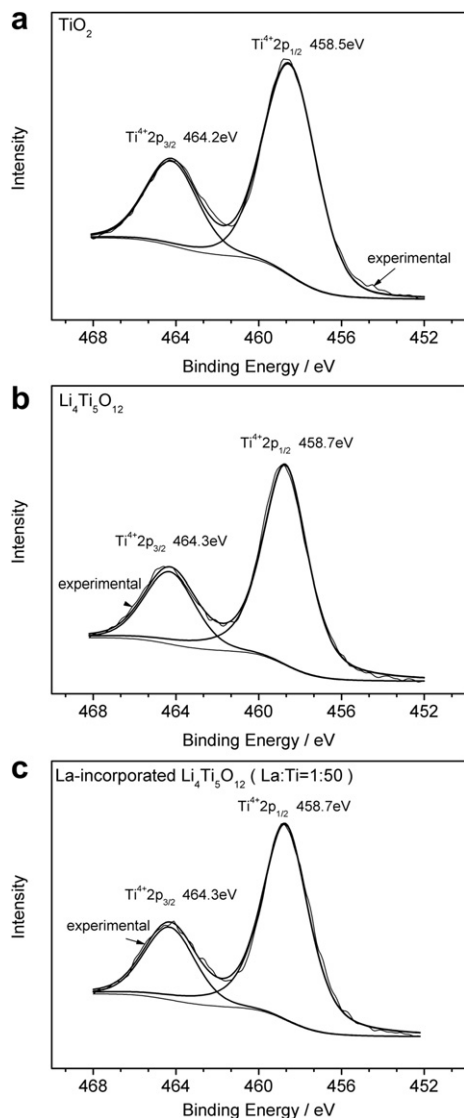**Fig. 7.** The XPS images of (a) commercial TiO_2; (b) pure $Li_4Ti_5O_{12}$; (c) La-incorporated $Li_4Ti_5O_{12}$ (La:Ti = 1:50).

reported by Masanobu Nakayama et al. [39], the lanthanum lithium titanate can be reduced at around 1.5 V. However, the doping amount in our experiment was few and the lithium insertion capacity of lanthanum lithium titanate was low compared with $Li_4Ti_5O_{12}$. Thus we assumed that the effect of lanthanum lithium

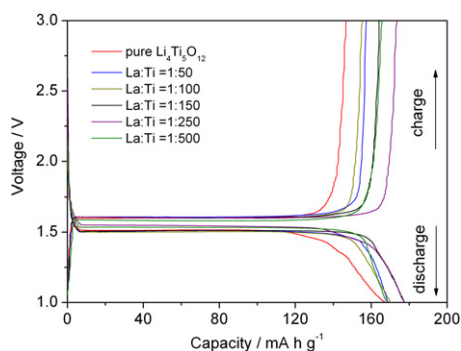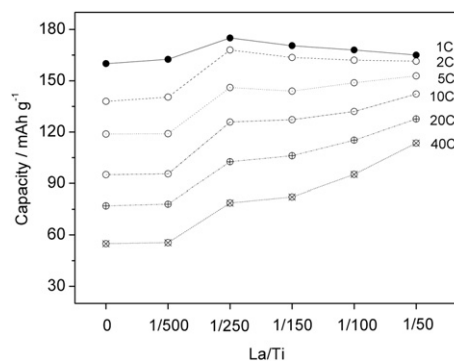**Fig. 9.** The rate performance of as-prepared La-$Li_4Ti_5O_{12}$ at various discharge rates with different La to Ti ratios.

titanate on the electrochemical behavior due to its reduction at 1.5 V was slight.

Fig. 9 shows the dependence of discharge capacity on the La to Ti molar ratio in the composites at various discharge rates, during each cycling process the charge and discharge rates were kept the same. Similar to that at 1 C rate, the discharge capacity first increased with La to Ti molar ratio to reach the maximum at La to Ti molar ratio of 1:250 and then decreased with the further increase in La to Ti molar ratio at the discharge rate of 2 C. However, with the further augment of discharge rate, a monotonous growing in discharge capacity was observed with the increasing La to Ti molar ratio. And the higher the discharge rate the more obvious beneficial effect in retaining the capacity was demonstrated. It indicates that the formation of lithium lanthanum titanate-$Li_4Ti_5O_{12}$ composite electrode improved the rate performance. A high discharge capacity of around 113.5 mA h g^{-1} was still reached at a 40 C rate for La-incorporated $Li_4Ti_5O_{12}$ electrode with La to Ti molar ratio of 1:50. The result is highly attractive by considering the coarse and pore-free nature of the secondary particles with a specific surface area of only 5.9 m^2 g^{-1}. Although comparable rate capacity was also reported in literature by other authors, their $Li_4Ti_5O_{12}$ electrodes always had high specific surface area (>60 m^2 g^{-1}) or possessed hierarchical 3D porous architectures through complicated advanced synthesis [25,40–42]. Fig. 10 shows the cycling stability of La-incorporated $Li_4Ti_5O_{12}$ electrode (La:Ti = 1:50) at a charge–discharge rate of 10 C. The capacity after the 150 times of cycling still reached 111.3 mA h g^{-1}, with capacity retention as high as 98%.

3.4. Mechanism analysis

It was reported that some two-phase boundaries can facilitate lithium storage by introducing pseudocapacitive effect [43,44].
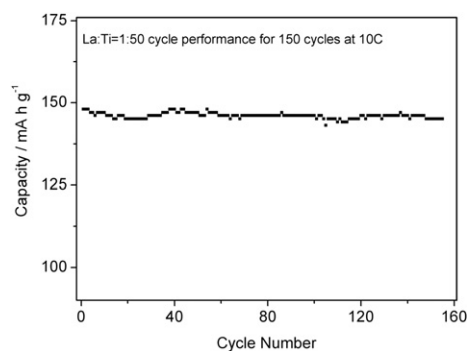

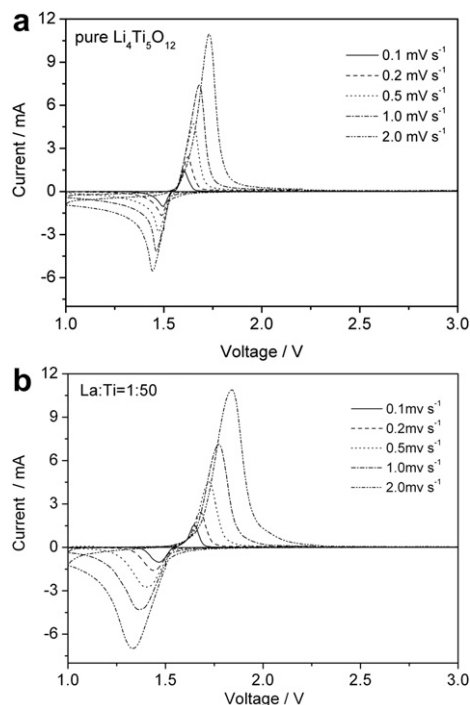**Fig. 8.** The initial charge and discharge curves for the as-prepared samples with different La to Ti ratios.

Fig. 10. The cycling performance of La-incorporated $Li_4Ti_5O_{12}$ with La-to-Li molar ratio of 1:50 at a charge–discharge rate of 10 C.

**Fig. 11.** Cyclic voltammograms of the as-prepared (a) pure $Li_4Ti_5O_{12}$ and (b) La-incorporated $Li_4Ti_5O_{12}$ (La:Ti = 1:50) at different scan rates of 0.1, 0.2, 0.5, 1.0, 2.0 mV s^{-1}.

Cyclic Voltammetry (CV) has been frequently applied to investigate the lithium insertion process of many electrodes. Generally, the sweep current i and scan rate v follow a simple power law of $i = av^b$, where both a and b are adjustable parameters [45]. There are two

well-defined conditions. If the b value is around 0.5, the electrode reaction was limited by diffusion process, under which the current is proportional to the square root of the scan rate v, while a linear relationship of i versus square root of v will be observed at $b = 1.0$, indicating a capacitive response. Fig. 11 shows the typical CV curves for pristine $Li_4Ti_5O_{12}$ and La-incorporated $Li_4Ti_5O_{12}$ (La to Ti molar ratio of 1:50) at various scan rates. Fig. 12 further shows the dependence of cathodic/anodic peak current i from the CV on scan rate v and square root of scan rat $v^{1/2}$ for pristine $Li_4Ti_5O_{12}$ and La-incorporated $Li_4Ti_5O_{12}$ with La to Ti molar ratio of 1:50. For the pristine $Li_4Ti_5O_{12}$, the peak current showed good linear relationship to $v^{1/2}$ (Fig. 12b), suggesting the lithium bulk diffusion played significant role in the electrode reaction, which can be explained by the long diffusion distance in the coarse grains. As to La-incorporated $Li_4Ti_5O_{12}$ with La to Ti molar ratio of 1:50, a linear dependence of peak current i on the scan rate v was clearly demonstrated as shown in Fig. 12c. It suggests the La-incorporated $Li_4Ti_5O_{12}$ electrode performed more like a pseudocapacitor. Clearly, the large amount of $Li_4Ti_5O_{12}$-lithium lanthanum titanate two-phase boundaries in the La-incorporated $Li_4Ti_5O_{12}$ (La to Ti molar ratio of 1:50) accounted for the appearance of such pseudocapacitive effect, which may likely enhance the surface charge transfer, and thus the rate capacity. Meanwhile, the apparent cathodic/anodic zone broadening and potential shift at the peak current in Fig. 11b compared with Fig. 11a can be attributed to the pseudocapacitive effect, which can be more detailed explained as the combination of pseudocapacitive response current peak and the reversible cathodic/anodic current peak of $Li_4Ti_5O_{12}$.

The EIS of various electrodes were measured and the results in Nyquist plots were presented in Fig. 13. During the test, the composite electrodes were first discharged to around 1.6 V and then equilibrated at this potential for several hours before the EIS were measured within the frequency range of 10^5–10^{-2} Hz. The impedance spectra are composed of a depressed semi cycle at the
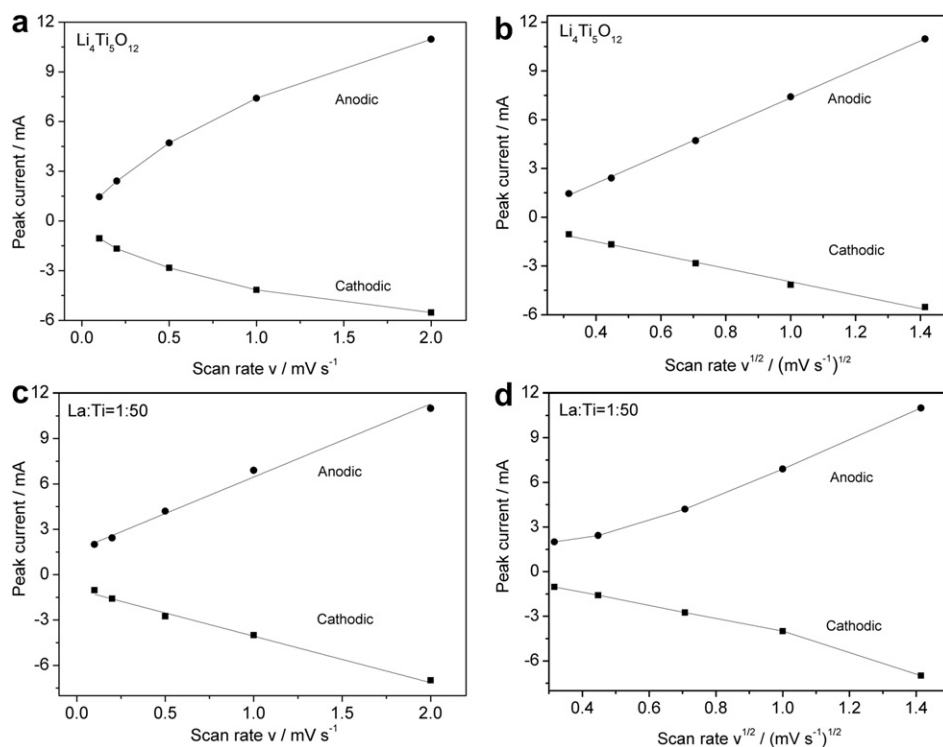
Fig. 12. The relationships between the peak current and scan rate v or $v^{1/2}$ in the cathodic/anodic processes of the (a–b) as-prepared pure $Li_4Ti_5O_{12}$ and (c–d) La-incorporated $Li_4Ti_5O_{12}$ (La:Ti = 1:50).
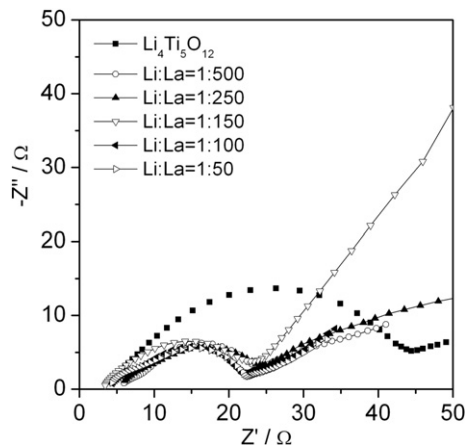
Fig. 13. Nyquist plots of the as-prepared La-Li$_4$Ti$_5$O$_{12}$ with different La to Ti ratios at the potential of 1.6 V within the frequency range of 10^5–10^{-2} Hz.

high-to-medium frequency range and a linear tail at the low frequency range. The intercept of the depressed semi cycle with the real axis at the high frequency can be attributed to the ohmic resistance of the liquid electrolyte, while the depressed arc is related with the charge transfer at the electrode liquid electrolyte interface and the corresponding capacitance. The linear tail at the low frequency embodies the Warburg diffusion resistance, which is related to the lithium diffusion within the oxide bulk. It was found that the electrode polarization resistance was indeed decreased after the incorporation of La into Li$_4$Ti$_5$O$_{12}$.

Lithium lanthanum titanate is A-site cation deficient perovskite oxides with lithium-ion conductivity as high as ∼10^{-3} S cm^{-1} at room temperature [28,29]. The formation of lithium lanthanum titanate solid electrolyte–Li$_4$Ti$_5$O$_{12}$ composite may also increase the apparent lithium-ion conductivity, which will contribute additionally to the improved rate performance by reducing bulk diffusion polarization resistance during the lithium insertion and extraction processes. The diffusion coefficient ($\tilde{D}$) of lithium ion in the electrode materials can be calculated using following equation [46]:

$$\tilde{D} = \left[\frac{V_m(dE/dx)}{\sqrt{2}AzFa} \right]^2$$

In which V_m is the molar volume of the electrode (the volume of 45.73 cm^3 mol^{-1} for pristine Li$_4$Ti$_5$O$_{12}$), w is frequency, $j = \sqrt{-1}$. The parameters were adopted for all electrodes in this study. dE/dx is the slope of potential at 1.6 V versus x which can be calculated from
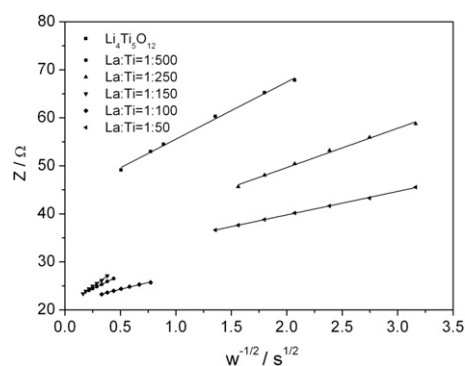

Fig. 14. The real parts of the complex impedance vs. $w^{1/2}$ at potentials about 1.6 V with different La to Ti mole ratios.

Table 1
Values of A, dE/dx and $\bar{D}$ correspond to the voltage of 1.6 V with different La to Ti ratios.

Samples	A	dE/dx	$\bar{D}$ (cm^2 s^{-1})
Li$_4$Ti$_5$O$_{12}$	11.2	5.0	9.5×10^{-9}
1:500	10.7	5.6	1.3×10^{-8}
1:250	7.9	4.6	1.6×10^{-8}
1:150	6.6	6.2	6.6×10^{-8}
1:100	5.9	4.6	2.9×10^{-8}
1:50	4.8	4.7	4.6×10^{-8}

the first discharge curve. The pre-exponential factor A is a constant which can be calculated from the relationships between the resistance and frequency at a selected voltage. z is the charge transfer number in lithium-ion battery z is 1, a is the surface area of the active electrode (here is 1.54 cm^2), F is the Faradic constant (here is 9.6485×10^{-4} C mol^{-1}), and $\tilde{D}$ is the average lithium diffusion coefficient. Fig. 14 shows the dependence of the Z versus $w^{-1/2}$ at 1.6 V. From the slope, A, dE/dx and then $\tilde{D}$ can be obtained, and the results are listed in Table 1. The diffusion coefficient ($\tilde{D}$) of pristine lithium is 9.5×10^{-9} cm^2 s^{-1}, which matched well with our previous report and other authors [47,48]. As expected, a monotonous increase in $\tilde{D}$ with La to Ti molar ratio was observed, and a value of 4.6×10^{-8} cm^2 s^{-1} was found for La-Li$_4$Ti$_5$O$_{12}$ with La:Ti = 1:50, which is almost 5 times that of pristine Li$_4$Ti$_5$O$_{12}$.

Based on above analysis, a mechanism for the formation of the composite with rich lithium lanthanum titanate–Li$_4$Ti$_5$O$_{12}$ dual phase boundaries from the combustion synthesis and the improved rate performance of the as-synthesized coarse La-incorporated Li$_4$Ti$_5$O$_{12}$ as compared to the pristine Li$_4$Ti$_5$O$_{12}$ was proposed, which is schematically shown in Fig. 15. During the combustion synthesis, the in-situ formation of lithium lanthanum titanate and Li$_4$Ti$_5$O$_{12}$ occurred simultaneously. Due to the molecular level mixing of the raw materials, the two phases are well mixed to result in tremendous lithium lanthanum titanate–Li$_4$Ti$_5$O$_{12}$ dual phase boundaries in nano domains. During the phase formation, partial La^{3+} also incorporated into Li$_4$Ti$_5$O$_{12}$ to cause the displacement of Ti^{4+} from 16d site into 8a site. The creation of fast lithium-ionic conductor lithium lanthanum titanate in the composite effectively improved the apparent lithium conductivity of the electrodes, and the displacement of Ti^{4+} into the 8a Li$^+$ tetrahedral site increased the electronic conductivity of the oxide, both facilitated the bulk diffusion. On the other hand, the rich lithium lanthanum titanate–Li$_4$Ti$_5$O$_{12}$ phase boundaries in the composites increased the surface kinetics to provide a faster surface charge transfer. As a result,
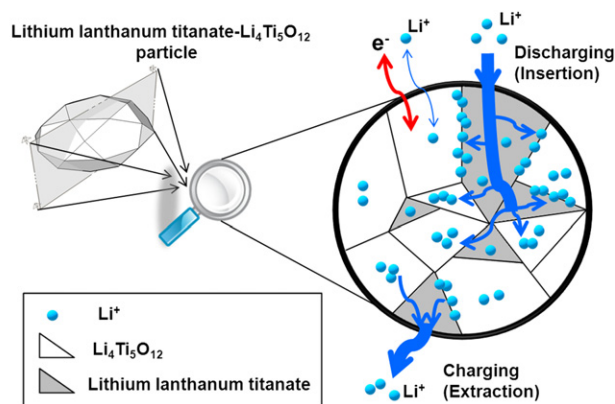

Fig. 15. Schematic illustration for the electrochemical reaction path on lithium lanthanum titanate–Li$_4$Ti$_5$O$_{12}$ particle.

improved rate capacity was observed for the coarse electrode. The small specific surface area and also free from SEI due to the high discharge voltage accounted for the small irreversible capacity during the first charge–discharge cycling of the various La-$Li_4Ti_5O_{12}$ composites. Furthermore, the solid electrolyte phase in the composite effectively reduced the electrode–liquid electrolyte interface, in combination with the negligible volumetric change of lithium insertion and extraction processes of $Li_4Ti_5O_{12}$, consequently leading to the high cycling stability.

4. Conclusions

From above analysis, it was clear that La-incorporated $Li_4Ti_5O_{12}$ prepared from combustion synthesis showed multiple advantages, which account for the high rate performance and excellent stability of the as-prepared coarse electrodes. The formation solid electrolyte–electrode composite in nano domains to improve the rate performance is a general concept, which may also be applicable to other electrode materials such as $LiFePO_4$. We expect that this concept will open up a new way for the development of high rate performance electrodes, which may greatly accelerate the commercialization of EVs and HEVs and contribute significantly to a sustainable future.

Acknowledgments

References

[1] A.G. Ritchie, J. Power Sources 96 (2001) 1–4.
[2] B. Kang, G. Ceder, Nature 458 (2009) 190–193.
[3] F.G. Cheng, J. Liang, Z.L. Tao, J. Chen, Adv. Mater. 23 (2011) 1695–1715.
[4] Z.G. Yang, J.L. Zhang, M.C.W. Kintner-Meyer, X.C. Lu, D.W. Choi, J.P. Lemmon, J. Liu, Chem. Rev. 115 (2011) 3577–3613.
[5] R. Marom, S.F. Amalraj, N. Leifer, D. Jacob, D. Aurbach, J. Mater. Chem. 21 (2011) 9938–9954.
[6] J. Leadbetter, L.G. Swan, J. Power Sources 216 (2012) 376–386.
[7] A.M. Skundin, O.N. Efimov, O.V. Yarmolenko, Russ. Chem. Rev. 71 (2002) 329–346.
[8] V. Etacheri, R. Marom, R. Elazari, G. Salitra, D. Aurbach, Energy Environ. Sci. 4 (2011) 3243–3262.
[9] B. Scrosati, J. Hassoun, Y.K. Sun, Energy Environ. Sci. 4 (2011) 3287–3295.
[10] G. Jeong, Y.U. Kim, H. Kim, Y.J. Kim, H.J. Sohn, Energy Environ. Sci. 4 (2011) 1986–2002.
[11] J.R. Owen, Chem. Soc. Rev. 26 (1997) 259–267.
[12] J.B. Goodenough, Y. Kim, Chem. Mater. 22 (2009) 587–603.
[13] P.G. Bruce, B. Scrosati, J.M. Tarascon, Angew. Chem. Int. Ed. 47 (2008) 2930–2946.
[14] J. Gao, J.R. Ying, C.Y. Jiang, C.R. Wan, J. Power Sources 166 (2007) 255–259.
[15] A.S. Aricò, P. Bruce, B. Scrosati, J.M. Tarascon, W.V. Schalkwijk, Nat. Mater. 4 (2005) 366–377.
[16] Y.G. Guo, J.S. Hu, L.J. Wan, Adv. Mater. 20 (2008) 2878–2887.
[17] J. Haetge, P. Hartmann, K. Brezesinski, J. Janek, T. Brezesinski, Chem. Mater. 23 (2011) 4384–4393.
[18] N. Ohta, K. Takada, L.Q. Zhang, R.Z. Ma, M. Osada, T. Sasaki, Adv. Mater. 18 (2006) 2226–2229.
[19] Y.G. Wang, H.Q. Li, P. He, E. Hosono, H.S. Zhou, Nanoscale 2 (2010) 1294–1305.
[20] C.H. Jiang, M. Ichihara, I. Honma, H.S. Zhou, J. Power Sources 52 (2007) 6470–6475.
[21] Y.G. Wang, H.M. Liu, K.X. Wang, H. Eiji, Y.R. Wang, H.S. Zhou, J. Mater. Chem. 19 (2009) 6789–6795.
[22] L. Cheng, J. Yan, G.N. Zhu, J.Y. Luo, C.X. Wang, Y.Y. Xia, J. Mater. Chem. 20 (2009) 595–602.
[23] D. Wang, N. Ding, X.H. Song, C.H. Chen, J. Mater. Sci. 44 (2009) 198–203.
[24] L. Kavan, M. Gratzel, Electrochem. Solid-State Lett. 5 (2002) A39–A42.
[25] L.F. Shen, C.Z. Yuan, H.J. Luo, X.G. Zhang, K. Xu, Y.Y. Xia, J. Mater. Chem. 20 (2010) 6998–7004.
[26] H.G. Jung, S.T. Myung, C.S. Yoon, S.B. Son, K.H. Oh, K. Amine, B. Scrosati, Y.K. Sun, Energy Environ. Sci. 4 (2011) 1345–1351.
[27] T. Yuan, R. Cai, K. Wang, R. Ran, S.M. Liu, Z.P. Shao, Ceram. Int. 35 (2009) 1757–1768.
[28] S. Stramare, V. Thangadurai, W. Weppner, Chem. Mater. 15 (2003) 3974–3990.
[29] P. Knauth, Solid State Ion. 180 (2009) 911–916.
[30] S.H. Huang, Z.Y. Wen, X.J. Zhu, Z.H. Gu, Electrochem. Commun. 6 (2004) 1093–1097.
[31] Z.J. Ding, L. Zhao, L.M. Suo, Y. Jiao, S. Meng, Y.S. Hu, Z.X. Wang, L.Q. Chen, Phys. Chem. Chem. Phys. 13 (2011) 15127–15133.
[32] S.H. Huang, Z.Y. Wen, J.C. Zhang, X.L. Yang, Electrochim. Acta 52 (2007) 3704–3708.
[33] T. Tabuchi, H. Yasuda, M. Yamachi, J. Power Sources 162 (2005) 813–817.
[34] R. Cai, T. Yuan, R. Ran, X.Q. Liu, Z.P. Shao, Int. J. Energy Res. 35 (2011) 68–77.
[35] B.B. Tian, H.F. Xiang, L. Zhang, Z. Li, H.H. Wang, Electrochim. Acta 55 (2010) 5453–5458.
[36] R.D. Shannon, Acta Crystallogr. A32 (1976) 751–767.
[37] D.T. Liu, C.Y. Ouyang, J. Shu, J. Jiang, Z.X. Wang, L.Q. Chen, Phys. Status Solidi B 243 (2006) 1835–1841.
[38] T. Yuan, R. Cai, Z.P. Shao, J. Phys. Chem. C 115 (2011) 4943–4952.
[39] M. Nakayama, T. Usui, Y. Uchimoto, M. Wakihara, M. Yamamoto, J. Phys. Chem. B 109 (2005) 4135–4143.
[40] E.M. Sorensen, S.J. Barry, H.K. Jung, J.M. Rondinelli, J.T. Vaughey, K.R. Poeppelmeier, Chem. Mater. 18 (2006) 482–489.
[41] J.Z. Chen, L. Yang, S.H. Fang, Y.F. Tang, Electrochim. Acta 55 (2010) 6596–6600.
[42] L.F. Shen, C.Z. Yuan, H.J. Luo, X.G. Zhang, L. Chen, H.S. Li, J. Mater. Chem. 21 (2011) 14414–14416.
[43] C. Lai, Y.Y. Dou, X. Li, X.P. Gao, J. Power Sources 195 (2010) 3676–3679.
[44] X.W. Guo, X.P. Fang, Y. Mao, Zh.X. Wang, F. Wu, L.Q. Chen, J. Phys. Chem. C 115 (2011) 3803–3808.
[45] J. Wang, J. Polleux, J. Lim, B. Dunn, J. Phys. Chem. C 111 (2007) 14925–14931.
[46] T. Yuan, R. Cai, K. Wang, R. Ran, S.M. Liu, Z.P. Shao, Ceram. Int. 35 (2008) 1757–1768.
[47] Y.C. Chen, C.Y. Ouyang, L.J. Song, Z.L. Sun, Electrochim. Acta 56 (2011) 6084–6088.
[48] Y.H. Rho, K. Kanamura, J. Solid State Chem. 177 (2004) 2094–2100.